Fabric-Reinforced Functional Insoles with Superior Durability and Anti-fracture Properties for Energy Harvesting and AI-empowered Motion Monitoring

Yuanyuan Gao[1], Bingang Xu[1], Minyu Qiu[2], Zhenyu Li[1], Taosif Ahmed[1], Yujue Yang[1], Xiaoyang Guan[1], Hong Fu[2]*

[1]Nanotechnology Center, Research Institute for Intelligent Wearable Systems, The Hong Kong Polytechnic University, Hong Kong 999077, Hong Kong, People's Republic of China

[2]Department of Mathematics and Information Technology, The Education University of Hong Kong, Hong Kong 999077, Hong Kong, People's Republic of China

*Corresponding author; Email: tcxubg@polyu.edu.hk

Abstract

Functional triboelectric insoles hold promise for advancing self-powered wearable technologies. However, their durability is compromised by continuous compressive forces and friction, leading to surface abrasion and material fracturing. To address these challenges, we have developed an innovative fabric-reinforced structure combined with a dual-L backrest design that enhances anti-fracture capabilities and electric outputs while enabling AI-empowered motion monitoring. Polydimethylsiloxane (PDMS) is used as the negative triboelectric material with a dual-L backrest design, while insulated copper wire (icuW) serves as the positive triboelectric material with an annular structure design. These components are intricately nested to enable a multilayered friction pairing. The fabric-reinforced structure demonstrates excellent compressive rebound resilience, withstanding forces of at least 1,000 N. Our functional insole, featuring a fabric-reinforced dual-L backrest structure (FRdL-insole), efficiently harvests biomechanical energy with a peak power of 8,214 μW and maintains highly consistent performance after 10 washing cycles and 60,000 durability tests. It can power portable electronic devices such as digital watches, calculators, hygrometers, and LEDs. Enhanced with machine learning algorithms, the FRdL-insole processes sensor signals to monitor human movements, accurately identifying seven distinct motions. This positions the insole as a smart, real-time, self-powered tool for activity recognition, showcasing its potential in intelligent wearable technology.

Keywords: Triboelectric nanogenerator; Fabric-Reinforced Structures; Energy harvesting; Human motion recognition; Machine learning

1. Introduction

In recent years, the evolution of smart electronics has trended towards miniaturization, wearability, and multifunctionality[1-3]. Traditional electrochemical storage devices often fall short when it comes to power small-scale electronic devices, due to their inherent drawbacks such as limited lifespans, the necessity for frequent recharging, recycling challenges, and environmental concerns[4, 5]. This has precipitated an urgent demand for eco-friendly and sustainable energy alternatives[6-9]. Triboelectric nanogenerators (TENGs) have emerged as a formidable competitor in the field of energy harvesting. Wang et al. first proposed the concept of TENGs in 2012[10], which enables the conversion of irregular low-frequency mechanical energy from the environment into electricity, providing a new solution for the development of self-powered wearable electronic devices. TENGs are based on the coupling effect of electrostatic induction and triboelectrification, and it possesses favorable characteristics such as low manufacturing cost and a wide range of material choices [11-13]. Energy collection through TENGs can be achieved through human daily activities such as walking, tapping, jumping, friction, and touch. The energy harvested from human motion is green, environmentally friendly, safe, and sustainable[14-16]. Owing to its prominent advantages such as low cost, high conversion efficiency, and easy accessibility, TENGs have exhibited extensive applications in wearable device powering, multifunctional self-powered sensing and health monitoring, among other fields[17-20].

In the burgeoning field of wearable technology, the fusion of human biomechanics with advancements in material science plays a pivotal role, particularly in the sphere of energy-harvesting devices. Triboelectric insoles, which ingeniously convert the mechanical energy derived from human motion into electric energy, are at the vanguard of such technological breakthroughs[21-26]. These devices harness the natural movements of walking or running to generate power, offering a promising solution for self-sustained wearable electronics. To enhance the efficacy of TENGs, effort has been made across various dimensions, including the development of multilayer-stacked structures, nanostructured surface modifications, and the synthesis of novel contact materials[27-30]. Research works have also been directed towards optimizing surface charge density, refining mechanical designs, pioneering manufacturing techniques, and devising sophisticated power management circuits[31-38]. Despite the progress made in the field, the durability of triboelectric insoles remains a formidable challenge. Silica

gel, a material commonly used in triboelectric insole fabrication, provides commendable elasticity and rebound properties. However, due to their continuous exposure to compressive forces and friction, the longevity of these triboelectric insoles could be at risk. The cyclic high pressure and regular wear can result in degradation, such as surface abrasion, material fracturing, or a reduction in performance of the TENGs. Furthermore, despite silica gel's superior resilience and quick recovery characteristics, its propensity for shear and tear could significantly undermine its durability[39, 40].

To overcome the aforementioned challenges, we have designed and developed a novel fabric-reinforced structure combined with a dual-L backrest design that significantly enhances anti-fracture capabilities and boosts electrical output. The essence of this structure lies in the synergistic blend of fabric reinforcement and the inherent high resilience of silica gel, achieved through crosslinking and curing. Polydimethylsiloxane (PDMS) is used as the negative triboelectric material with a dual-L backrest design, while insulated copper wire (icuW) serves as the positive triboelectric material with an annular structure design. These components are intricately nested to enable a multilayered friction pairing. The fabric-reinforced functionality is achieved through an alternating coating of fabric and silica gel, with the option to vary the cotton fabric from zero to three layers. The inherent anisotropic properties of the fabric not only address cracking challenges but also allow for fine-tuning the silica gel's elasticity. This tunability is crucial for the prompt and repeated engagement and disengagement of the triboelectric elements, thereby facilitating efficient charge transfer and resulting in heightened electrical output. The fabric-reinforced structure demonstrates excellent compressive rebound resilience, withstanding forces of at least 1,000 N. Our functional insole, featuring a fabric-reinforced dual-L backrest structure (FRdL-insole), efficiently harvests biomechanical energy with a peak power output of 8,214 μW and maintains highly consistent performance even after 10 washing cycles and 60,000 durability tests. It can power portable electronic devices such as digital watches, calculators, hygrometers, and LEDs. Enhanced with machine learning algorithms, the functional insole processes sensor signals to monitor human movements, accurately identifying seven distinct motions. The FRdL-insole has proven to be an effective tool for both harvesting biomechanical energy and monitoring various human movements. This offers an exceptional wearable digital platform/system with potential applications in motion capture and monitoring, identification, and smart sports technologies.

2. Results and discussion

Structural design of functional insole. The structural design and fabrication method of the functional insole, featuring a fabric-reinforced dual-L backrest structure (FRdL-insole), are schematically illustrated in Fig. 1. Considering the motion patterns of human feet, there is a relatively large displacement space at the heel position. A fabric-reinforced dual-L backrest structure, as illustrated in Fig. 1a, is designed at this location. It utilizes Polydimethylsiloxane (PDMS) as the negative triboelectric material with a dual-L backrest design, while insulated copper wire (icuW) serves as the positive triboelectric material with an annular structure design. Fig. 1b presents a photograph of the fabric-reinforced dual-L backrest structure and the annular icuW. Fig. 1c provides a schematic of the structure and materials used in the fabric-reinforced structure. Silica gel and cotton fabric serve as the substrate for the fabric-reinforced structure through crosslinking and curing, with silver fabric (AgF) acting as the electrode and PDMS as the negative triboelectric material. PDMS is integrated with AgF (PDMS@AgF) via crosslinking and curing, as illustrated in Fig. 1d and e, which display the schematic diagram of PDMS@AgF and the structural formula of PDMS. The electrode layer AgF adopts a knitted structure that facilitates the adsorption of PDMS, and the cotton fabric used in the fabric-reinforced structure is of a high-strength woven structure (see Fig. S1a-c in the Supporting Information). To investigate the impact of fabric layers on elasticity adjustability and electrical performance, we prepared fabric-reinforced structures with different layers of cotton fabric. The detailed fabrication procedure is provided in the experimental section. Briefly, PDMS was scraped to the same height as that of the mold, and AgF was then tiled on the surface of PDMS in semi-crosslinked state, as shown in Fig. S2a. Subsequently, silica gel and cotton were coated in sequence, (cotton fabric ranging from 0-3 layers), as shown in Fig. S2b, and finally, the mold was removed after drying to obtain the fabric-reinforced structure ranging from without cotton fabric (F-0), 1 layer of cotton fabric (F-1), 2 layers of cotton fabric (F-2), to 3 layers of cotton fabric (F-3), integrated with the substrate and PDMS@AgF. F-0, a pure silica gel substrate, can achieve rapid rebound under the folded structure. However, it suffers from poor shear strength, making it prone to cracking and breakage, as shown in Fig. 1f and g. Owing to the synergistic blend of fabric reinforcement with the inherent high resilience of silica gel, the fabric-reinforced structure can resolve the problem of pure silica gel crack and growth under cyclic bending loads, as shown in Fig. 1h and i. Additionally, the number of fabric layers can adjust the elasticity of the silica gel, facilitating rapid contact and separation of the triboelectric materials, which is

beneficial for charge transfer and achieving high electric output. Fig. 1j and k show the scanning electron microscope (SEM) images of pure silica gel substrate and the fabric-reinforced structure of 2 layers of cotton fabric (F-2), respectively.

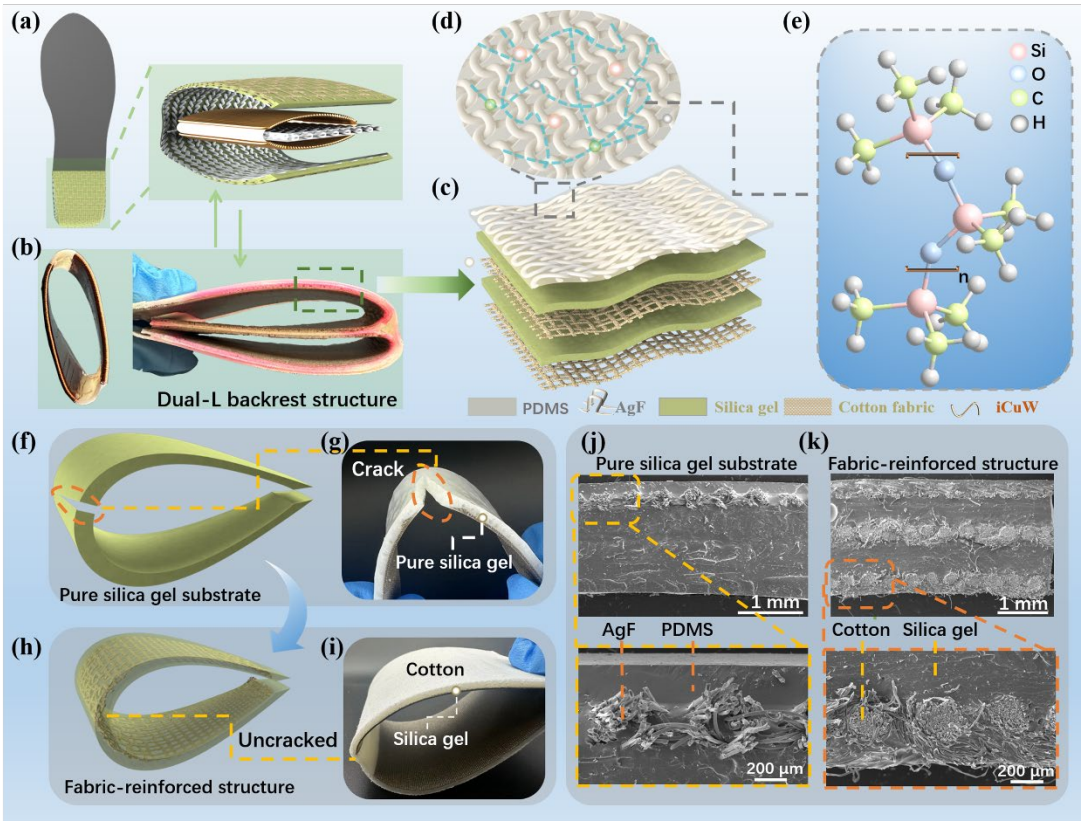

Fig. 1. Schematic diagram for design and fabrication of FRdL-insole. (a) Schematic diagram of FRdL-insole. (b) Photograph of fabric-reinforced dual-L backrest structure and annular icuW. (c) Material diagram of fabric-reinforced structure. (d) Schematic diagram of the PDMS@AgF. (e) Structural formula of PDMS. Comparison between (f) schematic diagram and (g) photograph of silica gel with crack, and (h) schematic diagram and (i) photograph of fabric-reinforced structure of F-2. SEM images of (j) pure silica gel substrate (top) of F-0 and its enlarged area (bottom) containing AgF@PDMS, (k) fabric-reinforced structure of F-2 (top) and its enlarged area (bottom) containing silica gel-coated cotton.

Working mechanisms of the FRdL-insoles. The working principle of the FRdL-insoles is illustrated in Fig. 2, which operates under a vertical contact and separation mode. PDMS serves as the negative triboelectric material, while icuW acts as the positive triboelectric material that is designed in between, as illustrated in Fig. 2a. Human movement initiates the contact and separation of the FRdL-insoles. In detail, upon compression of the FRdL-insoles (Fig. 2b-i), the negative triboelectric charges on the PDMS surface are completely balanced by the positive electrostatic charges generated on the icuW surface. As the compressive force is releasing (Fig. 2b-ii), the

icuW electrode progressively induces positive charges onto the PDMS electrode through electrostatic induction. This electric potential difference propels a electron flow, generating an instantaneous current. When the compressive is fully released (Fig. 2b-iii), PDMS and icuW achieve their maximum separation, and charge transfer stabilizes. When the FRdL-insoles are compressing (Fig. 2b-iv), the positive charges on the PDMS electrode revert to the icuW electrode to balance the potential difference, creating a current in the reverse direction until the system returns to its compressed state (Fig. 2b-i). Thus, an alternating current is cyclically produced via the contact and separation process under external loads. To elucidate the power generation mechanism, the potential distribution across the components is simulated using COMSOL, as demonstrated in Fig. 2c.

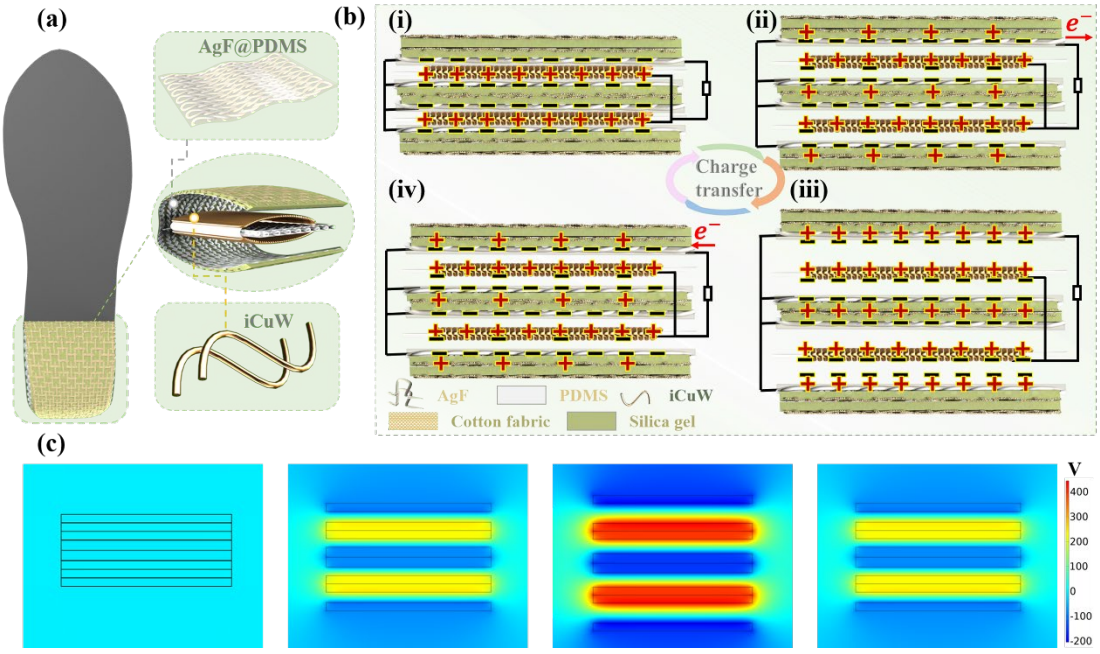

Fig. 2. Working mechanisms of the FRdL-insoles. (a) Schematic diagram of the FRdL-insoles. (b) Electricity generation mechanisms of the combination of the FRdL-insoles. (c) Simulation results for potential distribution of constituent components by COMSOL.

Mechanical property of the fabric-reinforced structure. To investigate the impact of fabric layers on elasticity adjustability, we evaluated mechanical properties of fabric-reinforced structures with different layers of cotton fabric, as shown in Fig. 3. The pure silica gel substrate is vulnerable to shearing and has a tendency to fracture. However, the fabric-reinforced structure can effectively prevent shear-induced cracks and significantly enhance its tensile strength. Fig. 3a-c illustrate the tensile properties of the

fabric-reinforced structure. The results of the tensile properties, as displayed in Fig. 3b, reveal that the fabric-reinforced structure substrate containing cotton fabrics (F-1, F-2, F-3) exhibit significantly higher strength than the pure silica gel structure (F-0), and the fracture strength increases with the increase of number of fabric layers in the fabric-reinforced structure. In addition, during the tensile process, the fabric-reinforced structural substrate completely breaks first, as shown in Fig. 3a. Subsequently, the triboelectric material tends to breaking due to the elasticity of AgF during the tensile process, exhibiting relatively low tensile strength at this stage, as illustrated in Fig. 3c which is a local magnification of curves shown in Fig. 3b. (see video 1 in the Supporting Information).

Furthermore, the silica gel permeates into the AgF and cotton fabric and undergoes crosslinking and curing at high temperatures. To assess the bonding strength of the fabric-reinforcement structure, we conducted peel tests on the bonding strength between AgF and silica gel, as well as between cotton fabric and silica gel, as shown in Fig. 3d and 3e. The fabric-reinforcement structure was cut into a rectangular shape with a width of 25 mm. The AgF and silica gel layers were pulled using a tensile tester (Instron 5566). The adhesion toughness was calculated by doubling the plateau force and dividing by the sample width[40]. The bonding strength of AgF with silica gel is approximately 580 N/m, as shown in Fig. 3d. Using the same method, we tested the adhesion toughness of the cotton fabric and silica gel. The cotton and silica gel layers were also pulled by a tensile tester, and the bonding strength was approximately 260 N/m, as shown in Fig. 3e. This indicates that the fabric-reinforcement structure exhibits stable and strong adhesion owing to the silica gel permeating the fabric and undergoing crosslinking and curing. Additionally, since the primary application of fabric-reinforced structures as insoles is subject to vertical compressive rebound forces, we studied the compressive performance of fabric-reinforced structures of F-0, F-1, F-2, and F-3. As shown in Fig. 3f, under a fixed compressive strain of 0.7, the rebound effect improves with an increasing number of fabric layers. Moreover, the pure silica gel structure (F-0) is prone to fracture under a compressive force of 1,000 N, as shown the enlarged part of the photographs in Fig. 3g, while the fabric-reinforced structure substrate containing fabric (F-1, F-2, F-3) maintain good compressive rebound capabilities under at least 1,000 N of force, as demonstrated in Fig. 3g.

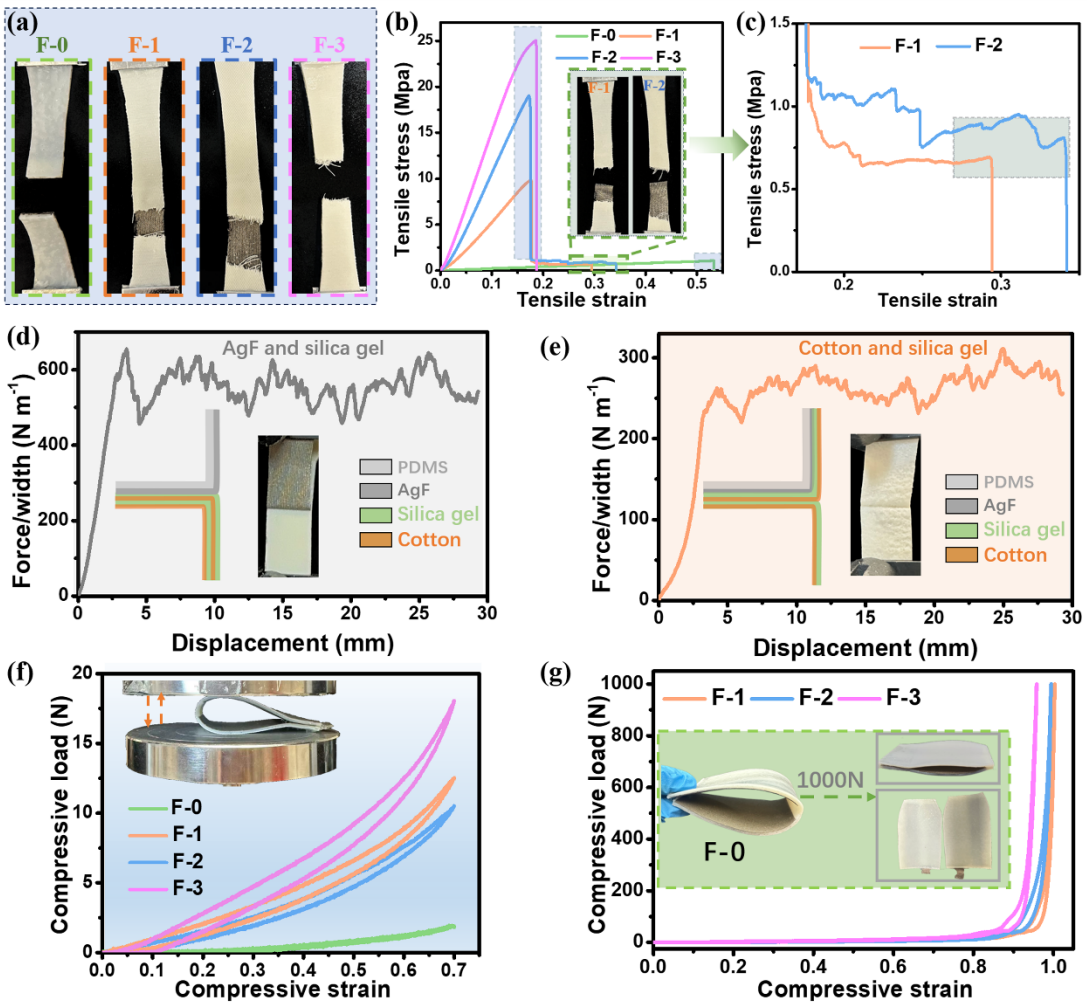

Fig. 3 Mechanical property of the fabric-reinforced structure. (a) The photographs of breaking, (b) tensile testing of the fabric-reinforced structures of F-0, F-1, F-2, and F-3 and (c) the enlarged area of containing tesile curves of F-1 and F-2. Force per unit width as a function of displacement during the peel test of (d) AgF and silica gel and (e) cotton fabric and silica gel. (f) Compression test of the fabric-reinforced structures of F-0, F-1, F-2, and F-3 at the strain of 0.7. (g) Compression test of the fabric-reinforced structures of F-1, F-2, and F-3 under a force of 1,000 N, and the insert shows the fracture of F-0 after the test.

Output performance evaluation of the fabric-reinforced structure. A systematic exploration was conducted to assess the biomechanical energy harvesting capabilities of fabric-reinforced structures by measuring their electric outputs with various materials and movement states. Specifically, with a constant frequency of 3 Hz and a force of 40 N, PDMS, renowned for its excellent electrical properties [41], was employed as the negative triboelectric material. It was paired with various positive triboelectric materials, including blended fabrics, nylon fabrics, copper-nickel conductive fabrics (CNF), and icuW, each with an area of 16 cm^2, as illustrated in Fig.

4a. As shown in Fig. 4b-d, icuW demonstrated superior electrical performance, generating a current of approximately 15 uA, a charge of around 370 nC, and a voltage of about 330 V. This was followed by CNF, nylon fabric, and blend fabric, which demonstrated currents of 11 uA, 9.5 uA, and 9.2 uA, charges of 306 nC, 267 nC, and 260 nC, and voltages of 305 V, 217 V, and 169 V respectively. Therefore, the icuW as positive triboelectric material will be used in the following studies.

Fig. 4e-h show the photographs of the front, back, side, and cross-section views of the fabric-reinforced structures of F-0, F-1, F-2, and F-3, each with a thickness of about 2.5 mm. The electric performance of the fabric-reinforced structures of F-0, F-1, F-2, and F-3 was assessed across various states of movement by individuals wearing the insole. An electrometer and oscilloscope were used to record the short-circuit current/charge and output voltage signals, as shown in Fig. S3 in the Supporting Information. As the number of fabric layers increased from 0 to 3, there was a gradual rise in the short-circuit current from approximately 14 uA to 30 uA, 25 uA to 45 uA and 38 uA to 59 uA, the output voltage from about 100 V to 260 V, 135 V to 314 V and 180 V to 355 V , and charge from about 146 nC to 425 nC, 170 nC to 450 nC and 185 nC to 455 nC during walking, jogging, and running, respectively, as shown in Fig. 4i-n and Fig. S4-S6 in the Supporting Information. The main reason for the increase in triboelectric properties is that, as the number of fabric layers increases, the structure's resilience improves. Improved resilience of the fabric-reinforced structure results in a faster movement during the contact-separation process. According to the formula in Supplementary Note 1 of the Supporting Information, this increased speed during the contact-separation process enhances the stimulation of external electron flow, potentially leading to a higher output[42-44]. As the number of fabric layers increases, the resilience of the structure improves, but this would compromise the comfort of the insole. The electric performance difference between the fabric-reinforced structures of F-2 and F-3 is not significant, but F-3 presents a slightly lower comfort level. Therefore, taking into account both superior electrical properties and wearing comfort, we have further integrated and optimized the fabric-reinforced structures of F-2 in the following studies.

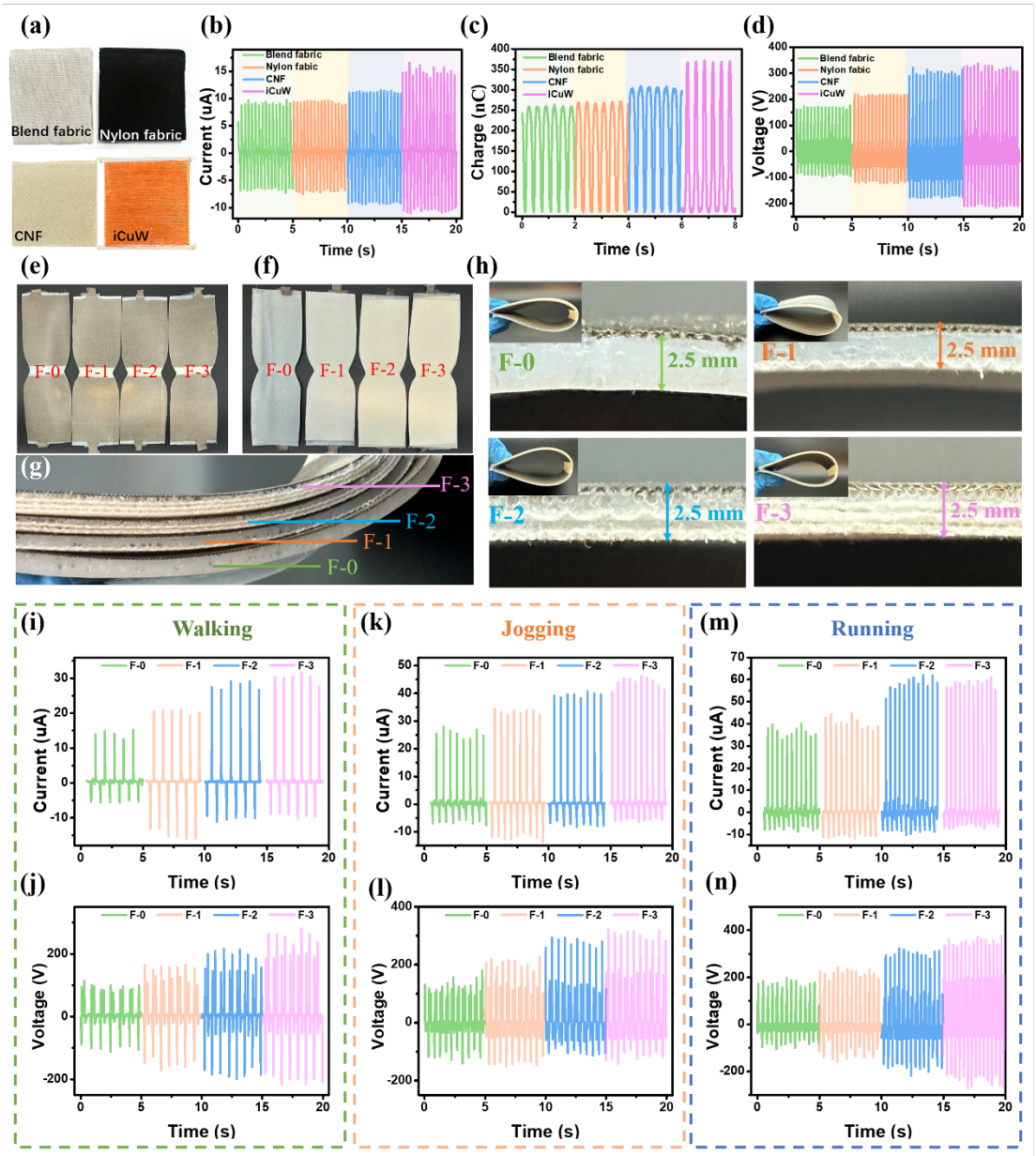

Fig. 4 (a) The photographs of positive triboelectric material. (b) Short-circuit current, (c) transferred charge and (d) output voltage of the positive triboelectric material and PDMS. (e) Front photographs, (f) back photographs, (g) side photographs and (h) cross section for fabric-reinforced structure of F-0, F-1, F-2 and F-3. (i) Short-circuit current and (j) output voltage during walking, (k) short-circuit current and (l) output voltage during jogging, (m) short-circuit current and (n) output voltage during running, for the fabric-reinforced structures of F-0, F-1, F-2, and F-3.

Based on the fabric-reinforced structure F-2, we further integrated and fabricated the corresponding FRdL-insole. The detailed fabrication procedure is provided in the experimental section and Fig. S7 of the Supporting Information. This design incorporates multiple triboelectric layers within a confined space to achieve improved electrical performance. The schematic diagram of the FRdL structure is depicted in Fig.

5a. The integration process of the FRdL-insole is illustrated in Fig. 5b. The negative triboelectric material, PDMS, features a dual L-shaped design to increase the contact area. The positive triboelectric material, icuW, features an annular structure design, and silica gel-coated cotton serves as the annular substrate to enhance elastic recovery. The positive and negative triboelectric materials are intricately nested to facilitate a multilayered friction pairing. We conducted a comparative analysis of the voltage, charge, and current for both FRdL-insole and fabric-reinforced structure F-2 under walking, jogging, and running conditions, as shown in Fig. 5c-e. Compared with F-2, the current of FRdL-insole was significantly increased by approximately 43%, 31%, and 26% for walking, jogging, and running, respectively. Similarly, the charge was increased by 41%, 40%, and 34%, and the voltage was increased by over 44%, 19%, and 17% for the same activities, respectively. These improvements are primarily owing to the increased contact area. The power outputs of FRdL-insole and F-2 were also evaluated by connecting them to a series of external resistances. Under jogging conditions, different resistors ranging from 1 KΩ to 3 GΩ were externally connected to test the output current. It can be seen that output current of FRdL-insole and F-2 were decreases gradually with the increase of resistance, as shown in Fig. S8 in Supporting Information, which follows the Ohm's law. The instantaneous peak power of FRdL-insole and F-2 was calculated using the formula $P = I^2R$, where P represents power, I is the output current, and R denotes the external resistance for FRdL-insole and F-2, respectively. As shown in Fig. 5f, the power of a single FRdL-insole and F-2 reaches a peak value of 8,214 μW and 5,400 μW, respectively, at an external resistance of 6 MΩ. And the FRdL-insole will be used in the following studies.

Moreover, reliability and washability are also the important requirements of insoles in practical applications. To evaluate the reliability of FRdL-insole in practical applications, the output durability of the FRdL-insole was also tested at a frequency of 5 Hz and force of 30 N. The output current of FRdL-insole is stable and reproducible over 60,000 cycles, indicating a fascinating durability (Fig. 5g). In order to study the performance after washing, FRdL-insole was scrubbed by hand with commercial detergent in water like common insole. The electric performance in different washing cycles is shown in Fig. 5h. It turns out that the electrical output of FRdL-insole remains stable even after 10 times of washing. To evaluate the practical wearing experience of the FRdL-insole, we evaluated the output performance during sweat accumulation while wearing the device. 384 mg artificial sweat[45, 46] was sprayed onto the FRdL-

insole every 5 minutes over a 1-hour measurement period. As shown in Fig. S9, the FRdL-insole exhibits a much slower decline in output as sweat volume increases, with nearly 83% of the output remaining even after 1 hour of slow walking. To further confirm its practical application potential. We tested the charge under different humidity and temperature conditions. As shown in Fig. R10, at a given impact force of 30 N and a frequency of 5 Hz, the charge decreased to 89% as the humidity increased from 40% to 70% (Fig. S10a). When the temperature increased from 20°C to 50°C, there was a slight upward trend of electrical properties (Fig. S10b). Based on these results, the FRdL-insole is applicable and reliable across a wide range of humidity and temperature conditions for energy harvesting. As compared with previous works, our FRdL-insole exhibited a comparable and even higher electrical performance, as shown in Table S1 in Supporting Information[21, 28, 47-52].

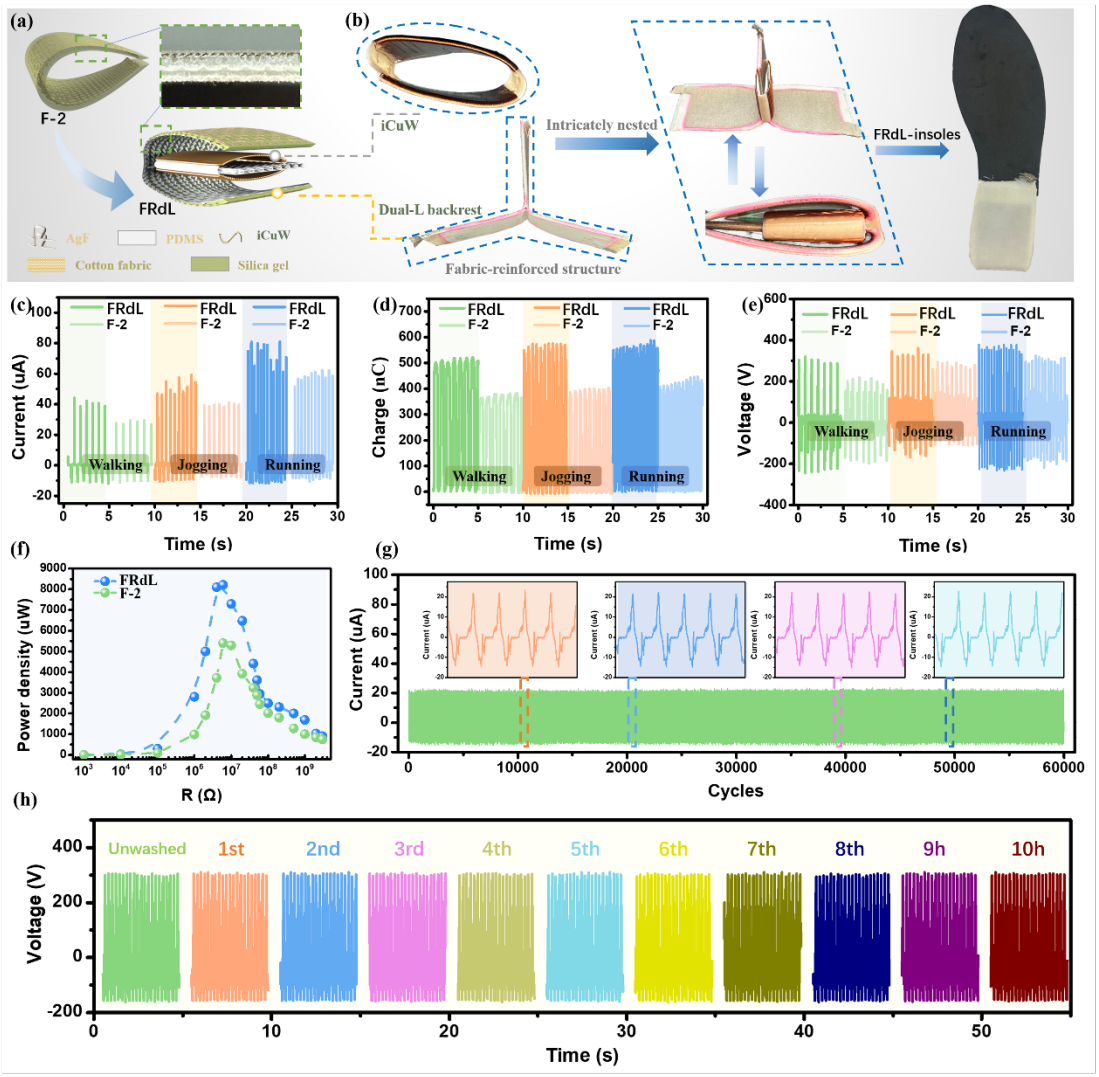

Fig. 5 (a) Schematic diagram of FRdL structure. (b) The integrated process of FRdL-insole. Comparison of (c) Short-circuit current, (d) transferred charge (e) output voltage during

walking, jogging and running, and (f) the peak power performance between structure F-2 and FRdL-insole during jogging. (g) Durability measurement of FRdL-insole for 60,000 cycles. (h) Electric performance of the FRdL-insole in 10 cycles of washing.

Application of FRdL-insole. The FRdL-insole has been further developed for energy generation and self-powered sensing across various applications. The energy storage capabilities of the FRdL-insole were evaluated by charging a range of commercial capacitors from 1 μF to 100 μF. The equivalent circuit models for charge/discharge cycles and the corresponding charging profiles are depicted in Fig. 6a and Fig 6b. For capacitors rated at 1 μF and 4.7 μF, the charging time to reach 15 V was approximately 5 s and 25 s, respectively, with charging rates of 3 V/s and 0.6 V/s. Capacitors with values of 10 μF, 22 μF, 47 μF, and 100 μF achieved charge levels of 12 V, 6.7 V, 4 V, and 2 V within 60 s at rates of 0.2 V/s, 0.11 V/s, 0.07 V/s, and 0.03 V/s, respectively. These results highlight the FRdL-insole's significant potential to power a wide array of electronic devices. To validate the FRdL-insole's capability to energize commercial electronics, it was employed to power an electronic watch, a digital calculator, and a hygrometer. During a continuous jogging session, a 22 μF capacitor's voltage swiftly climbed from 0 to 2 V within 20 s using the FRdL-insole. The discharge of the capacitor was controlled via a switch, successfully powering the electronic watch and calculator, as illustrated in Fig. 6c and Fig. 6d (refer to videos 2 and 3 in the Supporting Information). Additionally, a commercial hygrometer was effectively powered under similar conditions using a 100 μF capacitor as the energy storage unit, as shown in Fig. 6e. Owing to its high electric outputs, the FRdL-insole can serve as a reliable and sustainable power source. The power generated by the FRdL-insole during jogging was used to illuminate over 468 LEDs, as demonstrated in Fig. 6f (see video 4 in the Supporting Information). These findings underscore the potential of the newly developed FRdL-insole as an efficient and eco-friendly energy solution.

Beyond its capabilities in energy harvesting, the FRdL-insole can also serve as a self-powered wearable sensor, offering rapid, real-time, and highly sensitive monitoring of various human body movements. Fig. 6g-h and Fig. S11 in the Supporting Information present both photographs and a schematic depiction of the FRdL-insole, showcasing its integration with Bluetooth wireless technology and software for the seamless wireless tracking of human motion. When worn, the FRdL-insole detects the wearer's movements, generating a real-time output voltage that is wirelessly transmitted to a smartphone via Bluetooth. This enables the smartphone to wirelessly track and monitor

human activities. Fig. 6i-n display images of the FRdL-insole serving as a sensor, and the voltage signals corresponding to various human motions such as walking, jogging, running, jumping, sitting, and squatting (see video 5 in the Supporting Information). The FRdL-insole proves to be an effective tool for the self-powered, real-time monitoring of human movements, highlighting its versatility and potential in wearable technology applications.

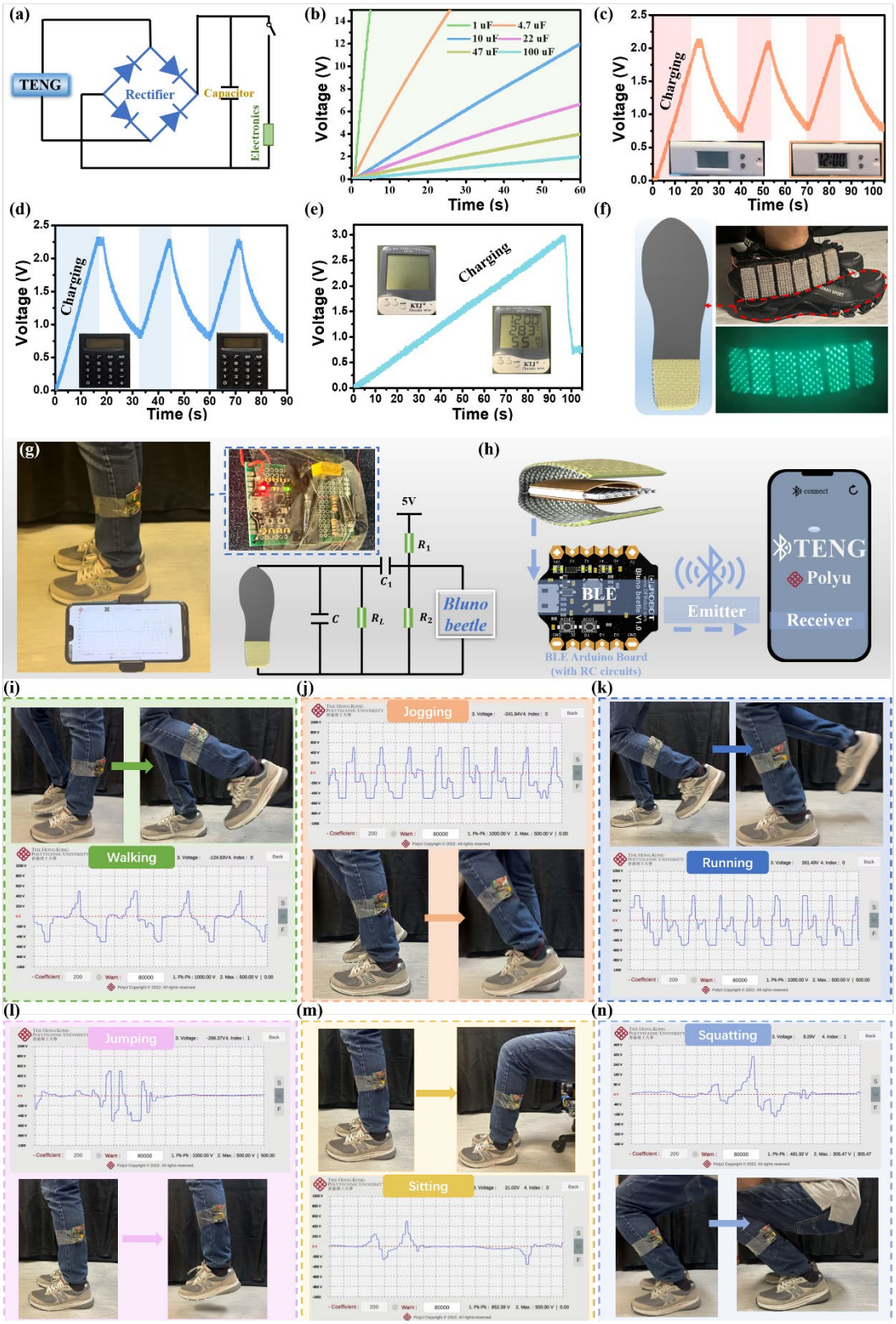

Fig. 6 (a) The equivalent circuit of charging/discharging of electronics. (b) Charging curves of 1 μF, 4.7 μF, 10 μF, 22 μF, 47 μF and 100 μF capacitors charged by the FRdL-insole during jogging. (c) Powering a commercial electronic watch with a 22 μF capacitor and (d) a digital calculator with a 22 μF capacitor and (e) hygrometer with a 100 μF capacitor by the FRdL-insole during jogging. (f) 468 green LEDs were directly lighted up by the FRdL-insole. (g) The

photographs and schematic illustration of FRdL-insole working as sensors with a Bluetooth board to connect smartphone. (h) The schematic illustration of the FRdL-insole as a self-powered sensor. The photographs and voltage signals of the FRdL-insole under conditions of (i) walking, (j) jogging, (k) running, (l) jumping, (m) sitting and (n) squatting.

In recent years, machine learning has surged forward as a cutting-edge tool for discerning subtle variations and handling complex signals[53, 54]. Deep learning, a particularly promising branch of machine learning, has been widely adopted for its robust adaptability and exceptional accuracy in analyzing diverse sensory data[55, 56]. Within this domain, one-dimensional convolutional neural networks (1D CNNs) have proven to be highly effective in extracting intricate features from time-series sensory data[57-59]. It typically consists of an input layer, several hidden layers like convolutional layers, pooling layers (Supplementary Note 2 of the Supporting Information), and an output layer. Leveraging the triboelectric signals captured from human movements by the FRdL-insole, a wearable motion recognition system was developed for distinguishing various human states with precision.

The schematic of data acquisition and triboelectric signals for various human motions is depicted in Fig. 7a. The initial step involves constructing a comprehensive database. Individuals' signals are collected using an electrometer data acquisition system. Fig. 7a displays the triboelectric signals associated with activities such as walking, jogging, running, jumping, sitting, squatting, and falling down. Subsequently, the FRdL-insole's signals are recorded, capturing over 500,000 data points for each type of motion. These motions are performed for more than 100 cycles. To ensure data collection, each action is recorded for a minimum duration of 500 seconds (see Fig. S12-S15 in Supporting Information), to compile the dataset. Of this dataset, 80% is allocated for training purposes, while the remaining 20% is reserved for testing. After gathering an extensive array of motion data from users, we proceed to construct the 1D CNN-based recognition motion model, as outlined in Fig. 7b. The network architecture consists of three convolutional layers, each followed by a max pooling layer to reduce the dimensionality and extract key features from the input sequence data. After the feature extraction stages, the model employs a fully connected layer to integrate these features and output predictions across seven human motion states. The samples are standardized and split into training and test sets in an 8:2 ratio to develop the detection model for the FRdL-insole. This division ensures a robust training foundation and an effective evaluation of the model's performance.

As illustrated in Fig. 7c, the model achieves an accuracy of approximately 90% at epoch 10, indicating its exceptional learning capabilities. With the increase in epochs, the model's accuracy continues to improve and eventually stabilizes, reflecting the high sensitivity of the FRdL-insole. Fig. 7d shows that the model's loss diminishes with the rising number of epochs and ultimately levels off near 0. To more clearly demonstrate the model's performance, Fig. 7e presents the classification results and confusion matrix of the 1D CNN for various motions. Utilizing the 1D CNN model, a high recognition accuracy of 96% is attainable, effectively distinguishing different types of motion. The accuracy for correctly classifying segments of falling down, jogging, jumping, running, sitting, squatting, and walking reached a pretty high level of 93%, 96%, 94%, 98%, 94%, 98%, and 100%, respectively. The accuracy is primarily influenced by the similarity of data across different labels; the more alike the data, the higher the potential for confusion. Misclassifications mainly arise from the difficulty in differentiating between falling down and sitting, as well as between jogging and jumping. For better understanding, we have supplemented this with motion prediction experiments, as shown in Fig. S16. Under unknown motion conditions, data is collected using an electrometer and processed through the CNN-based recognition motion model to obtain output results. Fig. S16a and S16b show the motion recognition results under walking and running conditions (see video 6 in the Supporting Information). To study the impact of body weight on identification accuracy, we included motion predictions for different body weights, as shown in Fig. S17. We collected data for body weights of 50kg, 60kg, and 70kg under walking conditions, and predicted the results using the 1D CNN-based motion recognition model, achieving accuracies of 1, 0.95, and 0.95, respectively. The accuracy could be further enhanced by expanding the training set with additional samples.

Moreover, we have added predictions regarding the plantar pressure and movement speed of the FRdL-insole. The current under different forces—light, medium, and strong—is shown in Fig. S18a-c. Using the 1D CNN model, an accuracy of approximately 90% is achieved by epoch 10 and the model's loss decreases as the number of epochs increases, as illustrated in Fig. S18d and S18e. Fig. S18f presents the classification results and confusion matrix of the 1D CNN for various forces, achieving a high recognition accuracy of 96%, effectively distinguishing different plantar pressures. From the enlarged view (Fig. S19a-ii) of Fig. S19a-i, the time interval between two positive/negative peaks can be extracted by the algorithm, allowing the

corresponding real-time motion speed to be calculated using a known step distance of 90 cm, as shown in Fig. S19a-iii. Additionally, motion steps and average speed can be obtained by counting the output peaks, with the results displayed in Fig. S19a-iv. Similarly, cases of fast walking and running are demonstrated in Fig. S19b and S19c, respectively. As compared with previous works, our FRdL-insole exhibited a comparable and even higher durability, identification accuracy and withstanding force, as shown in Table S2 in Supporting Information[23, 45, 53, 54, 60-62]. The metrics underscore the efficacy of the developed sensor and the CNN model in activity monitoring. Accurate activity monitoring is particularly valuable for the real-time assessment of critical patients, such as the elderly. Analyzing walking patterns can provide crucial insights for fall detection in elderly patients, enabling swift intervention for their safety. Moreover, integrating activity monitoring with machine learning facilitates the generation of periodic data, which can be leveraged to develop tailored exercise regimens, walking routines, body weight transformation charts, enhancing personal health management.

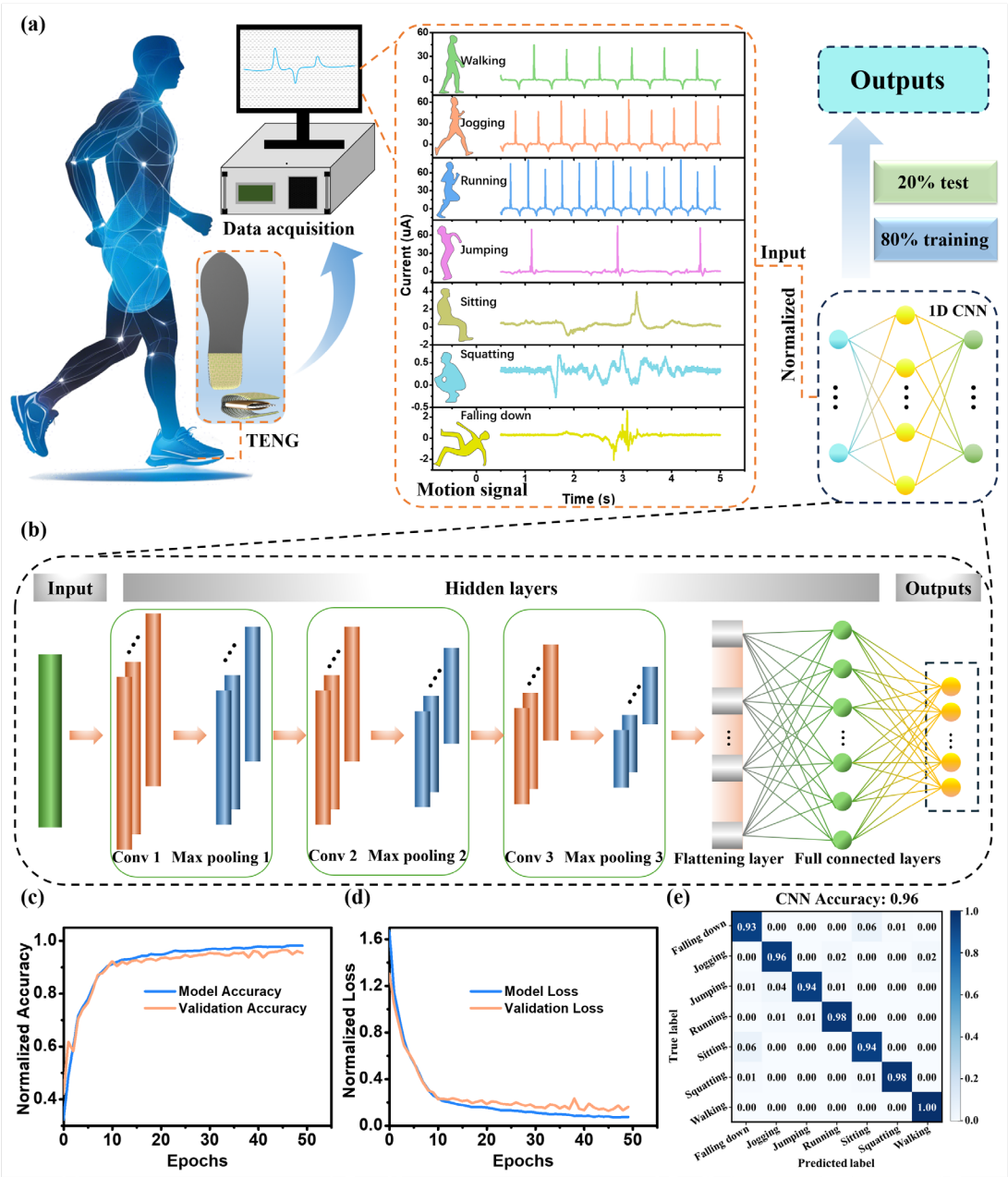

Fig. 7 Motion recognition based on the FRdL-insole empowered with deep learning. (a) The schematic flow from data acquisition to recognition of signals for different human motions. (b) Schematics of the process for constructing the 1D CNN structure. (c) Training and validation accuracy during 50 training epochs. (d) Training and validation loss during 50 training epochs. (e) Confusion map on test set.

3. Conclusion

In summary, we have designed and developed an innovative kind of fabric-reinforced functional insoles with superior durability and anti-fracture properties to significantly enhance anti-fracture properties and boost the electric outputs for energy harvesting and AI-empowered human motion monitoring. The fabric-reinforced structure exhibits

excellent compressive rebound resilience, withstanding forces of at least 1,000 N. For practical application, we designed the FRdL-insole based fabric-reinforced structure, which not only efficiently harvests biomechanical energy with a peak power of 8,214 μW but also maintains highly consistent electric performance after 10 washing cycles and 60,000 durability tests. It is capable of powering a commercial electronic watch, calculator, hygrometer, and LEDs. With the integration of machine learning algorithms, the FRdL-insole is adept at processing sensor signals to monitor human movements, accurately identifying seven distinct motions: walking, jogging, running, jumping, sitting, squatting, and falling. The showcased FRdL-insole has demonstrated high recognition accuracy, showing great potential as an intelligent, real-time, and self-powered device for the recognition of human activities.

Experiment section

Materials

AgF was purchased from Qingdao Hengtong X-silver Speciality Textile Co., Ltd. CNF was purchased from 3 M Corp. PDMS (Sylgard 184) was obtained from Dow Corning. Silica gel (ELASTOSIL LR 6200) was purchased from Wacker Chemie AG. Ordinary blend fabric (PET/cotton blend fabric), nylon fabric, and cotton fabric was purchased from the market. IcuW and CNF was purchased from the TaoBao. All the materials were used as received without any further purification.

Fabrication of fabric-reinforced structure

The PDMS was prepared by adding PDMS base and curing agent at a ratio of 10:1. After stirring for 3 mins, it was kept at room temperature for 30 mins to remove the bubbles. Then, the PDMS was poured into the mold, and the liquid thickness was evenly scraped to 0.5 mm with a glass rod. After the mold was dried in a 70 ℃ oven for about 10 mins to a semi-cross-linked state, AgF was tiled on the surface of PDMS as an electrode. Then, the mold was again dried in a 70°C oven for about 30 mins to fully cure the PDMS to obtain PDMS@AgF. Then, A solution and B solution of silica gel are mixed with the weight ratio of 1:1.

1) F-0

Incorporating a 2 mm thick mold atop the previously cured PDMS@AgF layer. Silica gel is then poured into this mold, and a blade coating technique, utilizing a glass tube or similar tools, is employed to ensure even distribution. The setup is kept at room temperature for 1 or 2 hours to remove the bubbles. Subsequently, it is placed in an oven at 70℃ for approximately 3 hours t to achieve curing. Finally, the mold is stripped

to obtain F-0 with a thickness of 2.5 mm.

1) F-1

Incorporating a 2 mm thick mold atop the previously cured PDMS@AgF layer. Silica gel is then poured into this mold, and a blade coating technique, utilizing a glass tube or similar tools, is employed to ensure even distribution. A layer of cotton fabric with a thickness of 0.45 mm is placed over the silica gel surface, ensuring complete saturation by the silica gel. Repeat the drying process of F-0 to obtain F-1 with a thickness of 2.5 mm.

2) F-2

Incorporating a 1 mm thick mold atop the previously cured PDMS@AgF layer. Silica gel is then poured into this mold, and a blade coating technique, utilizing a glass tube or similar tools, is employed to ensure even distribution. A layer of cotton fabric with 0.45 mm thickness is placed over the silica gel surface, ensuring it is fully saturated by the silica gel. This process is repeated by adding another 1 mm thick mold on top of the existing setup, followed by pouring silica gel, blade coating, and covering with another layer of cotton fabric, which is again thoroughly soaked in silica gel to achieve the desired reinforcement. Repeat the drying process of F-0 to obtain F-2 with a thickness of 2.5 mm.

3) F-3

Incorporating a 0.5 mm thick mold atop the previously cured PDMS@AgF layer. Silica gel is then poured into this mold, and a blade coating technique, utilizing a glass tube or similar tools, is employed to ensure even distribution. A layer of cotton fabric with 0.45 mm thickness is placed over the silica gel surface, ensuring it is fully saturated by the silica gel. The process is repeated with 0.5 mm and 1 mm thick mold to build up the reinforcement to the desired level. Repeat the drying process of F-0 to obtain F-3 with a thickness of 2.5 mm.

Test of fabric-reinforced structure of F-0, F-1,F-2 and F-3

The fabric-reinforced structure F-0 is folded with one end secured. An icuW with a diameter of 0.2 mm is uniformly wound in a 4 x 4 cm pattern on a PP board, which is then suspended and fixed at the midpoint of the folded structure to facilitate contact and separation. The F-1, F-2, and F-3 undergo the same procedures as described above.

Fabrication of FRdL-insole

First, prepare F-1with two thickness of 1.5 mm using the above method on the first plate. Simultaneously, a 0.45 mm thick cotton fabric is adhered to the second plate. A mold with a 1 mm thickness is prepared on top of the cotton fabric. Silica gel is poured

into the mold and a blade coating technique, utilizing a glass tube or similar tools, is employed to ensure even distribution. The setup is kept at room temperature for 1 or 2 hours to remove the bubbles. The two fabric-reinforced structures of F-1, each with a thickness of 1.5 mm, are detached from the first plate and connected with a silica gel-coated cotton layer on the second plate, forming a dual-L backrest design (see Fig. S7 of the Supporting Information). PDMS-coated AgF serves as the negative triboelectric material, with the middle backrest section cross-linked with silicone. The cotton-coated silicone acts as the support for the fabric-reinforced structures. It is secured in place and placed on a table once again for a duration of 1 or 2 hours. Subsequently, the assembly is cured in an oven at a temperature of approximately 70°C for approximately 3 hours. Once the curing process is complete, the sample is removed from the second plate.

Cut a piece of cotton fabric measuring 4 x 10 cm and evenly coat its surface with silica gel. After allowing it to rest for 1 hour, place it in an oven to dry. Then, uniformly wrap 0.2 mm icuW around its surface, creating two areas each measuring 4 x 4 cm, with a 1 cm gap in between. Then, the material is folded into an annular structure and stitched securely, nested atop the "L" shape base. The ends are folded and stitched to the sponge structure at the forefoot, a process which secures them together, resulting in what we have named the 'FRdL-insoles'.

Characterizations and measurements

Electrical output performance of fabric-reinforced structure were evaluated by Keyboard Life Tester (ZXA03). The force signal was monitored by DAQ (Dewetron, Dewe-2600 DAQ system) at the same time. An electrometer (Keithley 6514) and oscilloscope (Keysight Infiniivision DSOX3024T) recorded short circuit current and output voltage signals. The mechanical property was measured by INSTRON 5566. The output voltage was measured by an oscilloscope. The washability test of insole-2.0-f-2 was referring to AATCC standard 135-2004.

CRediT authorship contribution statement

Yuanyuan Gao: Methodology, Investigation, Writing – original draft. **Bingang Xu:** Conceptualization, Methodology, Supervision, Writing – review & editing. **Minyu Qiu** Investigation, Resources. **Zhenyu Li:** Investigation, Resources. **Taosif Ahmed:** Investigation. **Yujue Yang:** Resources. **Xiaoyang Guan:** Resources. **Hong Fu**: Resources

Declaration of Competing Interest

The authors declare that they have no known competing financial interests or personal relationships that could have appeared to influence the work reported in this paper.

Acknowledgement

The authors would like to acknowledge the funding support from The Innovation and Technology Commission of Hong Kong (ITP/066/18TI) and The Hong Kong Polytechnic University (G-YWA2, 1-YXAK, 1-WZ1Y) for the work reported here.

References

[1] T.R. Ray, J. Choi, A.J. Bandodkar, S. Krishnan, P. Gutruf, L. Tian, R. Ghaffari, J.A. Rogers, *Chemical reviews* **2019**, 119, 5461-5533.

[2] Z. Li, B. Xu, J. Han, J. Huang, K.Y. Chung, *Advanced Energy Materials* **2021**, 11, 2101294.

[3] J. Wen, B. Xu, J. Zhou, Y. Chen, *Journal of Power Sources* **2018**, 402, 91-98.

[4] H. Lu, J. Hu, X. Wei, K. Zhang, X. Xiao, J. Zhao, Q. Hu, J. Yu, G. Zhou, B. Xu, *Nature Communications* **2023**, 14, 4435.

[5] X. Liu, F. Xu, Z. Li, Z. Liu, W. Yang, Y. Zhang, H. Fan, H.Y. Yang, *Coordination Chemistry Reviews* **2022**, 464, 214544.

[6] Y. Chen, Y. Cheng, Y. Jie, X. Cao, N. Wang, Z.L. Wang, *Energy & Environmental Science* **2019**, 12, 2678-2684.

[7] X. Guan, B. Xu, J. Gong, *Nano Energy* **2020**, 70, 104516.

[8] A. Nozariasbmarz, H. Collins, K. Dsouza, M.H. Polash, M. Hosseini, M. Hyland, J. Liu, A. Malhotra, F.M. Ortiz, F. Mohaddes, *Applied Energy* **2020**, 258, 114069.

[9] J. Gong, B. Xu, Y. Yang, M. Wu, B. Yang, *Advanced Materials* **2020**, 32, 1907948.

[10] F.-R. Fan, Z.-Q. Tian, Z.L. Wang, *Nano energy* **2012**, 1, 328-334.

[11] D.G. Dassanayaka, T.M. Alves, N.D. Wanasekara, I.G. Dharmasena, J. Ventura, *Advanced Functional Materials* **2022**, 32, 2205438.

[12] L. Zhao, C. Fang, B. Qin, X. Yang, P. Poechmueller, *Nano Energy* **2024**, 127, 109772.

[13] S. He, J. Dai, D. Wan, S. Sun, X. Yang, X. Xia, Y. Zi, *Science Advances* **2024**, 10, eado6793.

[14] C. Ye, S. Yang, J. Ren, S. Dong, L. Cao, Y. Pei, S. Ling, *ACS nano* **2022**, 16, 4415-4425.

[15] K. Dong, X. Peng, Z.L. Wang, *Advanced Materials* **2020**, 32, 1902549.

[16] L. Zhao, B. Qin, C. Fang, L. Liu, P. Poechmueller, X. Yang, *Chemical Engineering Journal* **2024**, 479, 147898.

[17] B. Baro, S. Khimhun, U. Das, S. Bayan, *Nano Energy* **2023**, 108, 108212.

[18] J. Liao, X. Dai, J. Han, J. Yang, Y. Wu, Y. Cao, Y. Qiu, Y. Wang, L.-B. Huang, H. Ni, *Nano Energy* **2024**, 121, 109252.

[19] M. Li, B. Xu, Z. Li, Y. Gao, Y. Yang, X. Huang, *Chemical Engineering Journal* **2022**, 450, 137491.

[20] Y. Tang, B. Xu, D. Tan, J. Han, Y. Gao, Z. Li, X. Liu, *Nano Energy* **2023**, 110, 108358.

[21] Z. Zhou, L. Weng, T. Tat, A. Libanori, Z. Lin, L. Ge, J. Yang, J. Chen, *ACS Nano* **2020**, 14, 14126-14133.

[22] S. Chen, T. Huang, H. Zuo, S. Qian, Y. Guo, L. Sun, D. Lei, Q. Wu, B. Zhu, C. He, *Advanced*

Functional Materials **2018**, 28, 1805108.
[23] S. Hu, H. Li, W. Lu, T. Han, Y. Xu, X. Shi, Z. Peng, X. Cao, *Advanced Functional Materials* **2024**, 2313458.
[24] Y. Wang, L. Chu, S. Meng, M. Yang, Y. Yu, X. Deng, C. Qi, T. Kong, Z. Liu, *Advanced Science* **2024**, 2401436.
[25] Z. Lin, Y. Wu, Q. He, C. Sun, E. Fan, Z. Zhou, M. Liu, W. Wei, J. Yang, *Nanoscale* **2019**, 11, 6802-6809.
[26] L. Zhao, X. Guo, Y. Pan, S. Jia, L. Liu, W.A. Daoud, P. Poechmueller, X. Yang, *InfoMat* **2024**, 6, e12520.
[27] Y. Gao, B. Xu, D. Tan, M. Li, Y. Wang, Y. Yang, *Chemical Engineering Journal* **2023**, 466, 143079.
[28] Y. Gao, Z. Li, B. Xu, M. Li, C. Jiang, X. Guan, Y. Yang, *Nano Energy* **2022**, 91, 106672.
[29] K. Tao, Z. Chen, H. Yi, R. Zhang, Q. Shen, J. Wu, L. Tang, K. Fan, Y. Fu, J. Miao, W. Yuan, *Nano-Micro Letters* **2021**, 13, 123.
[30] D. Tan, B. Xu, Y. Gao, Y. Tang, Y. Liu, Y. Yang, Z. Li, *Nano Energy* **2022**, 104, 107873.
[31] C. Chen, L. Chen, Z. Wu, H. Guo, W. Yu, Z. Du, Z.L. Wang, *Materials Today* **2020**, 32, 84-93.
[32] Y. Li, Z. Zhao, L. Liu, L. Zhou, D. Liu, S. Li, S. Chen, Y. Dai, J. Wang, Z.L. Wang, *Advanced Energy Materials* **2021**, 11, 2100050.
[33] X. Li, C. Jiang, Y. Ying, J. Ping, *Advanced Energy Materials* **2020**, 10, 2002001.
[34] W. Liu, Z. Wang, G. Wang, Q. Zeng, W. He, L. Liu, X. Wang, Y. Xi, H. Guo, C. Hu, *Nature communications* **2020**, 11, 1883.
[35] P. Bai, G. Zhu, Z.-H. Lin, Q. Jing, J. Chen, G. Zhang, J. Ma, Z.L. Wang, *ACS nano* **2013**, 7, 3713-3719.
[36] E. He, Y. Sun, X. Wang, H. Chen, B. Sun, B. Gu, W. Zhang, *Composites Part B: Engineering* **2020**, 200, 108244.
[37] L. Ma, R. Wu, S. Liu, A. Patil, H. Gong, J. Yi, F. Sheng, Y. Zhang, J. Wang, J. Wang, *Advanced materials* **2020**, 32, 2003897.
[38] L. Liu, J. Li, Z. Tian, H. Wu, S. Zhou, X. Chen, Y. Zhu, X. Yang, W. Ou-Yang, *Nano Today* **2024**, 57, 102319.
[39] J. Steck, J. Kim, Y. Kutsovsky, Z. Suo, *Nature* **2023**, 624, 303-308.
[40] Z. Chen, G. Zhang, Y. Luo, Z. Suo, *Proceedings of the National Academy of Sciences* **2024**, 121, e2322684121.
[41] Z. Zhao, L. Zhou, S. Li, D. Liu, Y. Li, Y. Gao, Y. Liu, Y. Dai, J. Wang, Z.L. Wang, *Nature communications* **2021**, 12, 4686.
[42] K. Dong, X. Peng, J. An, A.C. Wang, J. Luo, B. Sun, J. Wang, Z.L. Wang, *Nature communications* **2020**, 11, 2868.
[43] J. Shen, Z. Li, J. Yu, B. Ding, *Nano Energy* **2017**, 40, 282-288.
[44] X.-S. Zhang, M.-D. Han, R.-X. Wang, F.-Y. Zhu, Z.-H. Li, W. Wang, H.-X. Zhang, *Nano letters* **2013**, 13, 1168-1172.
[45] F. Wen, Z. Sun, T. He, Q. Shi, M. Zhu, Z. Zhang, L. Li, T. Zhang, C. Lee, *Advanced science* **2020**, 7, 2000261.
[46] N.A. Taylor, C.A. Machado-Moreira, *Extreme physiology & medicine* **2013**, 2, 1-30.
[47] Q. Qiu, M. Zhu, Z. Li, K. Qiu, X. Liu, J. Yu, B. Ding, *Nano Energy* **2019**, 58, 750-758.
[48] M. Zhu, Q. Shi, T. He, Z. Yi, Y. Ma, B. Yang, T. Chen, C. Lee, *ACS nano* **2019**, 13, 1940-1952.

[49] M. Lou, I. Abdalla, M. Zhu, X. Wei, J. Yu, Z. Li, B. Ding, *ACS applied materials & interfaces* **2020**, 12, 19965-19973.
[50] J. Yi, K. Dong, S. Shen, Y. Jiang, X. Peng, C. Ye, Z.L. Wang, *Nano-micro letters* **2021**, 13, 1-13.
[51] W. Wang, J. Zhou, S. Wang, F. Yuan, S. Liu, J. Zhang, X. Gong, *Nano Energy* **2022**, 91, 106657.
[52] I. Appamato, W. Bunriw, V. Harnchana, C. Siriwong, W. Mongkolthanaruk, P. Thongbai, C. Chanthad, A. Chompoosor, S. Ruangchai, T. Prada, V. Amornkitbamrung, *ACS Applied Materials & Interfaces* **2023**, 15, 973-983.
[53] T. Jin, Z. Sun, L. Li, Q. Zhang, M. Zhu, Z. Zhang, G. Yuan, T. Chen, Y. Tian, X. Hou, C. Lee, *Nature Communications* **2020**, 11, 5381.
[54] Y. Lu, H. Tian, J. Cheng, F. Zhu, B. Liu, S. Wei, L. Ji, Z.L. Wang, *Nature communications* **2022**, 13, 1401.
[55] R. Shang, H. Chen, X. Cai, X. Shi, Y. Yang, X. Wei, J. Wang, Y. Xu, *Advanced Materials Technologies* **2024**, 2301316.
[56] C. Xin, Z. Xu, X. Xie, H. Guo, Y. Peng, Z. Li, L. Liu, S. Xie, *Advanced Science* **2023**, 10, 2302443.
[57] S. Yu, X. Piao, N. Park, *Nature Communications* **2020**, 11, 4842.
[58] Z. Xie, Y. Wang, M. Yu, D. Yu, J. Lv, J. Yin, J. Liu, R. Wu, *Nano Energy* **2022**, 103, 107804.
[59] Y. Xiong, L. Luo, J. Yang, J. Han, Y. Liu, H. Jiao, S. Wu, L. Cheng, Z. Feng, J. Sun, *Nano Energy* **2023**, 107, 108137.
[60] Y. Luo, Z. Wang, J. Wang, X. Xiao, Q. Li, W. Ding, H.Y. Fu, *Nano Energy* **2021**, 89, 106330.
[61] F. Wen, Z. Zhang, T. He, C. Lee, *Nature communications* **2021**, 12, 5378.
[62] H. Fang, L. Wang, Z. Fu, L. Xu, W. Guo, J. Huang, Z.L. Wang, H. Wu, *Advanced Science* **2023**, 10, 2205960.